SANDIA REPORT

SAND2006-55685568

Continuous-Flow Detector for Rapid Pathogen Identification

Louise M. Barrett, Andrew J. Skulan, Anup K. Singh, Eric B. Cummings, Gregory J. Fiechtner

Prepared by
Sandia National Laboratories
Albuquerque, New Mexico 87185 and Livermore, California 94550

Sandia is a multiprogram laboratory operated by Sandia Corporation,
a Lockheed Martin Company, for the United States Department of Energy's
National Nuclear Security Administration under Contract DE-AC04-94AL85000.

Approved for public release; further dissemination unlimited.

Issued by Sandia National Laboratories, operated for the United States Department of Energy by Sandia Corporation.

Available to DOE and DOE contractors from
U.S. Department of Energy
Office of Scientific and Technical Information
P.O. Box 62
Oak Ridge, TN 37831

Telephone: (865) 576-8401
Facsimile: (865) 576-5728
E-Mail: reports@adonis.osti.gov
Online ordering: http://www.osti.gov/bridge

Available to the public from
U.S. Department of Commerce

National Technical Information Service
5285 Port Royal Rd.
Springfield, VA 22161

Telephone: (800) 553-6847
Facsimile: (703) 605-6900
E-Mail: orders@ntis.fedworld.gov
Online order: http://www.ntis.gov/help/ordermethods.asp?loc=7-4-0#online

Continuous-Flow Detector for Rapid Pathogen Identification

Louise M. Barrett, Andrew J. Skulan, Anup K. Singh, Eric B. Cummings, Gregory J. Fiechtner

Microfluidics
Sandia National Laboratories
P.O. Box 969
Livermore, California 94550-MS9292

ABSTRACT

This report describes the continued development of a low-power, portable detector for the rapid identification of pathogens such as B. anthracis and smallpox. Based on our successful demonstration of the continuous filter/concentrator inlet, we believe strongly that the inlet section will enable differentiation between viable and non-viable populations, between types of cells, and between pathogens and background contamination. Selective, continuous focusing of particles in a microstream enables highly selective and sensitive identification using fluorescently labeled antibodies and other receptors such as peptides, aptamers, or small ligands to minimize false positives. Processes such as mixing and lysing will also benefit from the highly localized particle streams. The concentrator is based on faceted prisms to contract microfluidic flows while maintaining uniform flowfields. The resulting interfaces, capable of high throughput, serve as high-, low-, and band-pass filters to direct selected bioparticles to a rapid, affinity-based detection system.

The proposed device is superior to existing array-based detectors as antibody-pathogen binding can be accomplished in seconds rather than tens of minutes or even hours. The system is being designed to interface with aerosol collectors under development by the National Laboratories or commercial systems. The focused stream is designed to be interrogated using diode lasers to differentiate pathogens by light scattering. Identification of particles is done using fluorescently labeled antibodies to tag the particles, followed by multiplexed laser-induced fluorescence (LIF) detection (achieved by labeling each antibody with a different dye).

Acknowledgments

The authors thank Boyd Wiedenman and John Brazzle (Sandia National Laboratories) for mask layout and design assistance. The authors also thank Susan Jamison, William Kleist, and George Sartor (Sandia National Laboratories) for chip construction. The authors thank Judith Rognlein (Sandia National Laboratories) for providing samples of labeled *B. subtilis*. The authors thank Blanca Lapizco-Encinas, Yolanda Fintschenko and Blake Simmons for discussions regarding trapping of cells in microfabricated post arrays. This work was supported by Sandia National Laboratories' Laboratory Directed Research and Development funding under the program management of Duane Lindner. Sandia is a multi-program laboratory operated by Sandia Corp., a Lockheed Martin Co., for the United States Department of Energy under Contract DE-AC04-94AL85000.

Contents

Figures

Chapter 1

Chapter 2

Nomenclature

Microfluidic

Dielectrophoresis,

sample preparation,

particles,

cells,

separation,

Bacillus subtilis

Introduction

In the present report, we describe a selective pathogen filter/concentrators that can operate continuously, without the need to implement trap-and-release methods. Chapter 1 describes the investigation of ideal electrokinetic flow through microchannels designed using the faceted prism methodology previously developed by us at Sandia. This forms an experimental basis from which to rationally design filter/concentrator devices. Chapter 2 describes the investigation of the selective concentrator which uses single, insulating ridges to construct a voltage-addressable flow splitter in which desired pathogens can be forced selectively to flow into an output port of choice.

A uniform-field design approach can improve the performance of micro-analytical, chip-based devices for a number of applications, including chromatography and sample preparation. The faceted-prism paradigm allows the design of microfluidic devices possessing spatially uniform fields in electrokinetically driven flows. We present the first quantitative study of the velocity fields obtained using faceted interfaces between deep and shallow channel sections in Chapter 1. Electrokinetic flows were generated in a series of wet-etch fabricated microfluidic channels. The resulting velocity fields were analyzed by particle image velocimetry and compared with simulations of the two-dimensional Laplace equation using both the designed channel geometry and the as-fabricated channel geometry. This analysis found localized differences between the designed and observed flow fields that were directly attributable to the limitations of isotropic substrate etching. Simulations using the as-fabricated channel geometry reproduced the experimental electrokinetic velocity field, quantitatively accounting for speed field variations due to the limits of the fabrication method. The electrokinetic speed fields were also compared to corresponding pressure-driven speed fields.

This research formed the experimental basis for a novel filter/separator for the dielectrophoretic manipulation of particles and cells described in Chapter 2. A two level isotropic etch of a glass substrate was used to create three-dimensional ridge-like structures in micron-sized channels. Due to the insulating properties of glass, locally patterned regions of nonuniform electric field form near the ridges when a DC field is applied along the channel. The ridges are designed using the method of faceted prisms, such that substantially uniform fields are produced on each side of the faceted interfaces that form each ridge. The dielectrophoretic force that results from the electric field gradient near the ridges is used to affect particle motion parallel to the ridges in the absence of a bulk pressure-driven flow. Trapping and deflection of particles, and continuous concentration and separation of Bacillus subtilis from a two-component sample mixture are demonstrated. The flow of Bacillus subtilis is restricted to a selected channel of a planar, multi-channel device as a result of negative dielectrophoresis arising from the presence of the insulating ridges when the applied electric field exceeds a threshold of 30 V/mm. Dielectrophoresis has a negligible impact on 200-nm diameter polystyrene particles under the same conditions.

The successful demonstration of the filter/concentrators has prompted us to move up the design of subsequent diagnostic microchannel sections. Mixers have been designed and constructed to mix either micron-sized bacteria or molecules. These are designed to match a wide range of filter fluid velocities. Substantial intellectual property has been developed, yielding filed patents and technical advances. We have also performed important fundamental research, which has been published in highly regarded scientific journals.

CHAPTER 1

1.1 Chapter 1 Introduction

Microfluidic devices promise to allow a broad range of chemical and medicinal analyses using small sample volumes in compact, cheap and easily manufactured devices.[1, 2] The development of multifunctional, highly integrated micro-total analysis systems (μTAS)[3-5] will require methodologies that allow rational channel design for the control of fluid flow.

A novel method of channel design is based on faceted prisms (Fig. 1).[6, 7] Faceted channels consist of a concatenation of ridges of distinct depths. An example ridge is illustrated in the three-dimensional drawing of Fig. 1a, in which a fluid enters via a deep channel section, passes through a shallow region formed by an insulating ridge and exits through a deep channel. A corresponding top view of the ridge is shown in Fig. 1b. Such geometries allow the generation of spatially-uniform flow fields in each channel section (inlet, outlet, each ridge segment) under ideal electrokinetic flow conditions. They utilize the variation in specific permeability that arises from the corresponding variation of channel depth, and use simple trigonometric relations to allow precision design of spatially-uniform electrokinetic flows in turns, flow displacers, flow splitters and more exotic geometries.

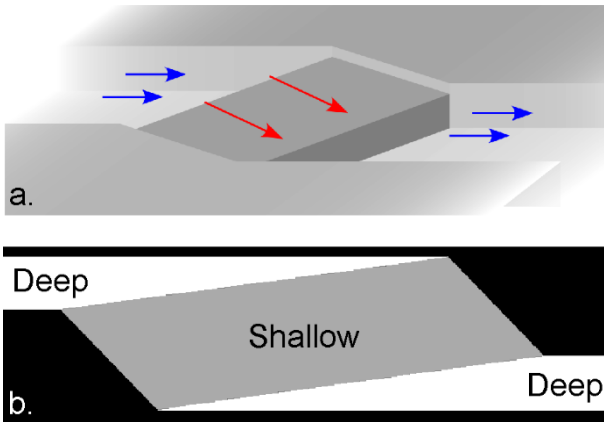

Figure 1. a. 3-dimensional illustration of a flow-displacer faceted channel, b. faceted-channel depth profile (top view). The blue arrows in the deep regions of (a) indicate a slower flow velocity relative to the shallow region above the ridge (red arrows).

A major design consideration in μTAS separation devices is dispersion minimization.[8] Under ideal conditions, a microfluidic separations element releases concentrated, fully resolved bands of each analyte. Experimentally, this efficiency is limited by diffusion, electric-field inhomogeneity and dispersion due to the channel geometry, decreasing the analytical resolution of these devices. Previous efforts to minimize this effect include: narrowing the channel at turns;[9-13] using complementary pairs of turns to cancel the dispersion in one turn;[14] using large-radius curves;[14-16] and differentially fabricating the side walls, either with coatings or geometrical obstructions to slow the flow on the inside of the curve and to compensate for the differences in path length.[17, 18] The faceted channel approach is ideally suited to addressing this problem and has been explored theoretically.[6, 7]

Other on-chip processes that can benefit from spatially-uniform flow designs are filtration and concentration, especially when this is performed using insulating dielectrophoresis (IDEP). IDEP arises when a gradient in an electric field is created by introducing insulating obstructions.[19-24] While these methods have displayed batch-wise concentration and separation, we have recently demonstrated continuous separation and concentration of a mixture of bacterial cells and latex nanospheres by a novel channel designed using the faceted prism design methodology.[25] This device operates in a voltage regime where the nonlinear dielectrophoretic contribution to particle motion is significant near the

interface between the deep channel and the shallow faceted prism. Other potential applications of the faceted prism methodology include flow splitters that minimize dispersion for applications such as multi-dimensional separations, or delivery to shallow channels for evanescent analyte detection with minimal dispersion.[7]

To create microfluidic devices, a number of micromanufacturing methods[26] (including wet-etching,[3, 27-30] laser ablation,[31, 32] embossing,[33-36] injection molding[37-39] and micromachining[40-42]) can be employed to construct channels containing ridges, each possessing practical limitations in precision. Because it is employed widely in the construction of μTAS devices,[3, 27, 29, 30, 43] and is readily available in our laboratory, the isotropic, wet-etching technique is used to construct channels in this study. Isotropic etching cannot generate sharp corners, rather forming rounded corners whose radii are proportional to the etch depth.[44]

In this paper we present the first experimental demonstration of the fields that result when using the faceted prism technique. The deviation from spatially-uniform flow behavior is examined for a series of faceted microchannels upon wet-etch device fabrication. The three channel geometries presented are: a straight, faceted channel, in which the faceted interface is perpendicular to the side walls; a flow displacer channel such as that shown in Fig. 1 that is useful in both flow control and concentration applications; and a flow divider that splits a fluid stream into two separate, parallel conduits. This deviation from ideal, spatially-uniform behavior due to a wet-etch fabrication method is reflected in variations of the velocity field. To our knowledge, this is the first presentation of the experimental examination of microchannels designed using a simple, field-based methodology. To assess the magnitude of the deviation from a spatially uniform velocity field by experimental means, particle-image velocimetry (PIV)[45-47] is used to obtain velocity fields. The resulting experimental velocity fields are compared to simulations of the Laplace equation based on the experimental geometries. The simulations serve as a tool to aid the analysis of the experimental velocity fields and verify that the deviations from spatially uniform fields are caused by limitations in fabrication rather than deviations from ideal electrokinetic flow.

Another factor that commonly interferes with pure electrokinetic velocity fields is pressure-driven flow.[48, 49] This is a difficult effect to eliminate, and becomes important during device operation as a result of reservoir-depth imbalance at microchannel inlet and outlet ports. Since our design methodology assumes the presence of ideal electrokinetic flow,[6, 7, 22, 50] we also examine the differences between pressure-driven and electrokinetic flows at a ridge.

1.2 Experimentals

1.2.1 Fabrication

The glass channels used in this study were designed and fabricated in-house using standard photolithography, wet-etch and bonding techniques. The microchips were fabricated from Schott D263 glass wafers (100-mm diameter, 1.1-mm thick, S. I. Howard Glass Company, Worcester, MA). The photomasks were designed using DW-2000 (Design Workshop Technologies., Montreal, Canada) and fabricated by Photo Sciences Inc., (Torrance, CA). D263 borosilicate wafers were sputter-deposited (Cooke Vacuum Products., South Norwalk, CT) with chromium metal to a thickness of 200 nm, which served as the hard mask. The mask defined a total of 16 channels of varying geometry, and each geometry was represented at least three times on the chip, for a total of 50 channels per chip. Three of these channel designs are described in this study. A 7.5-μm-thick layer of SJR 5740 (Shipley Corporation, Marlborough, MA) positive photoresist was spin-coated on the wafer and soft-baked at 90 °C for 5 min. The mask pattern was transferred to the photoresist by exposure to UV light in a contact

mask aligner at 775 μJ/mm^2. Exposure time varied depending on flux intensity (MA-6, Karl Suss America Inc., Waterbury Center, VA). After exposure, the photoresist was developed with Microposit developer concentrate (Shipley Corporation, Marlborough, MA) and hard-baked for 30 min at 125 °C. Exposed chromium was etched with CEN 300 Micro-chrome etchant (Microchrome Technologies Inc., San Jose, CA). The resulting exposed glass was etched with a 16% HF solution (Shape Products Company, Oakland, CA), and the remaining chrome was removed. This process was repeated to generate a two level etched device. The mask for the second etch was aligned with the first etch through the use of a pair of alignment marks located near the outer edges of the wafer. The alignment marks on the mask were overlaid with those on the wafer using a MA-6 Karl Suss aligner. The exposure time to the etchant was controlled to achieve a particular etch depth. The exposure time of the first etch was nine times that of the second etch, resulting in a device with deep channel ten times as deep as the facet depth. Via access holes were drilled in the cover plate (D263 Glass) with diamond-tipped drill bits (Amplex, Worcester, MA). The etched wafer and drilled cover plate was cleaned with 4:1 H_2SO_4/H_2O_2 (100 °C). The machined cover plate was rinsed with 1% HF solution to inhibit crack propagation. The substrates were then immersed into an 80 °C 40% NaOH solution, rinsed in a cascade bath, spun dry, aligned for contacting, and thermally bonded by slowly ramping the temperature to 610 °C for 5 h in a nitrogen-purged programmable muffle furnace (model 48000, Thermolyne, Dubuque, IA).

The channels consist of a facet located in the center of a 10.2-mm long channel (Fig. 2a). The inlet and outlet channels are accessed by 500-μL entrance and exit reservoirs. The designed facet depth is 5 μm (d_2 in Fig. 2c) and the channel depth is 50 μm (d_1 in Fig. 2c). The channel geometries display constant-radius curvature at the walls (Fig. 2b) where the radius equals the 50-μm etch depth (d_1 in Fig. 2c), which results from the use of an isotropic wet-etch during channel fabrication.

1.2.2 Data Acquisition and Reduction

The channels were filled with 200-nm diameter, green, fluorescently labeled latex beads (carboxylate modified FluoSpheres from Molecular Probes, Inc) diluted to 0.2% in deionized water (adjusted to pH = 7.83 with NaOH). Electrokinetic flows were generated by applying a voltage across a channel whose reservoirs had been volume-equilibrated to eliminate concurrent pressure-driven flow. Voltage was applied through two platinum electrodes attached to an E3630A power supply (Agilent Technologies, Inc, Palo Alto, CA). The applied potentials for the data presented are; straight (3 V/cm), displacer (6 V/cm) and splitter (3 V/cm). Pressure-driven flows were generated by making the reservoir volumes on the inlet and outlet channels unequal (head difference ~1 mm). Images of bead behavior were recorded using an IX70 inverted epifluorescence microscope with attached Cohu 4910 CCD camera (Cohu, Inc, San Diego, CA). CCD pixel size is 9 μm square. Microscope magnifications for images presented are; straight (x20), displacer (x10) and splitter (x20) channel, leading to spatial resolutions of 0.45, 0.90 and 0.45 μm, respectively. Following the approach of Meinhart et al,[51] we calculate a depth of correlation of 11.2 μm (x20) and 19.3 μm (x10) for our experimental setup. The focal plane is located at the center of the shallow facet in each experiment. Thus, for each channel geometry presented, the full cross-section of the shallow faceted region contributes to the PIV analysis. In the deep section, particles contribute to the PIV analysis if they are within 12.2 um (x10 objective) or 8.1 um (x20 objective) of the top of the channel. The successive image frames were recorded at 30 frames/second at 640 x 480 pixels/image.

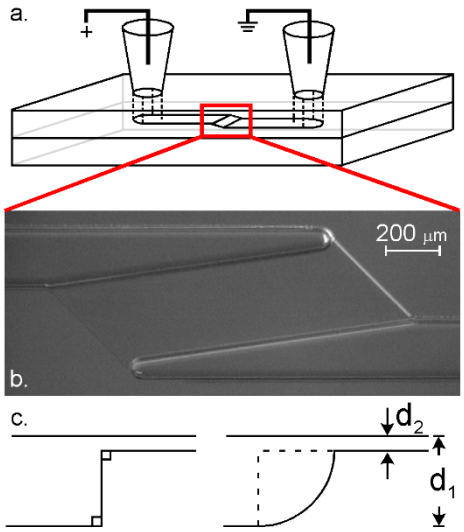

Figure 2. a. Microchannel geometry, including fluid reservoirs, b. top-illuminated image of the "displacer" channel, c. side-view illustration of an as-designed (left) and isotropic wet-etch ridge profile (right). The ratio of deep channel to ridge depth, d_1:d_2 is 10:1.

Successive image frames were analyzed using two pieces of software: the FlowManager Particle Image Velocimetry (PIV) software package (Dantec Dynamics, Inc) and a PIV code developed in-house.[47] For the FlowManager analysis, interpolations between successive frames were made using a cross-correlation method employing 16x16 pixel interrogation areas and requiring 75% overlap. Flow data for the first 5 seconds following the application of voltage were discarded as they may be distorted by initial flow equilibration or electric field stabilization. The images from the next ~20 seconds were averaged to generate the velocity fields presented below, resulting in greater than 250 correlated pairs of flow images contributing to each velocity field. The pressure-driven flow resulting from the pressure head generated by 25 seconds of electrokinetic flow was less than 3% of the electrokinetic velocity. To verify that the lower resolution PIV method delivered an accurate representation of the velocity field (e.g. near regions of sharp electric field gradients), the Sandia code was used and achieved single pixel resolution through a correlation-averaging approach. This process was repeated for multiple copies of the channels presented in this study on two separate chips.

1.2.3 Simulations

The electrokinetic flow was simulated using the Sandia "Laplace" electrokinetic and dielectrophoresis simulation code.[6, 7, 22, 52] The Laplace simulation package simulates ideal electrokinetic flows by solving the modified Laplace equation $\sigma(x,y)\nabla\varphi(x,y) = 0$ for the velocity/electrostatic potential φ on a quasiplanar domain defined by the field σ. This is applicable as the channel dimensions, applied potentials and other experimental variables approach the ideal electrokinetic limit.[53, 54] This allows the electrokinetic potentials (and their associated speed fields) to be described for a given channel geometry. The ideal geometries included three channel depths; wall (0 μm deep), inlet and outlet channels (50 μm deep) and facet (5 μm deep). The boundaries between these regions are sharp, reflecting the geometry shown in Fig. 1c, left. Simulations of the as-fabricated geometries possessed the same three depths, but gradients equal to the etch-depth were included at the boundaries between different depth regions, as required by isotropic etching (Fig. 2c, right). For convenience, this arc was approximated by a half-Gaussian curve.

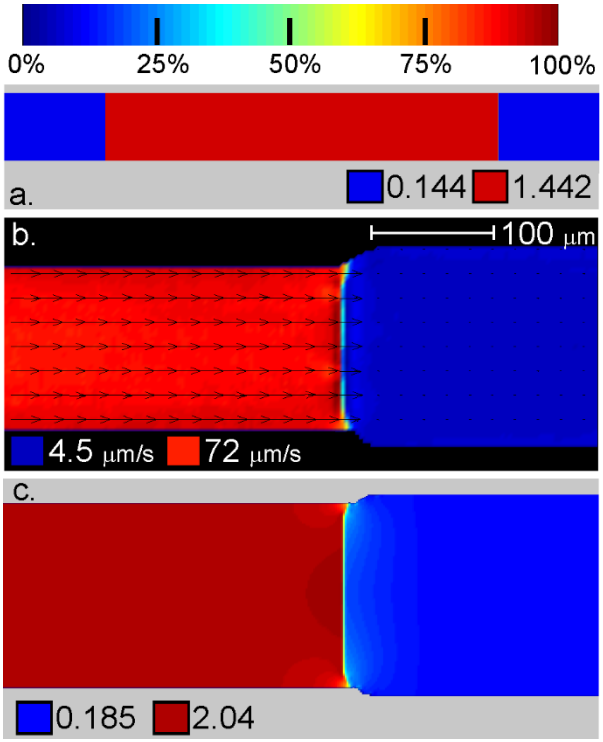

Figure 3. a. Laplace simulation of the as-designed straight-channel velocity field. The ratio of deep channel to ridge fluid depths in the simulation is 10:1. b. Experimental PIV velocity field of the 50:5 μm straight channel. c. Laplace simulation of the as-fabricated straight-channel velocity field. The simulation velocity is in arbitrary units. The look-up table (LUT) at the top of the figure is the same one used throughout this paper. Royal blue has a speed of 0 (in the appropriate units for the figure) while burgundy is 100% of the speed scale chosen for a particular figure.

1.3 Results and Analysis

1.3.1 Straight channel:

The simplest uniform-field channel design has faceted interfaces oriented perpendicular to the inlet and outlet channel walls.[6, 7] By employing this trivial design, the influence of complicating factors such as angled flows and rounded-turn corners can be eliminated from the study of velocity-field uniformity, allowing the impact of manufacturing offset and variability to be studied. The velocity field predicted by the Laplace simulation for such a trivial, ideal channel has two regions: a uniform, slow velocity in deep channel sections (depicted as blue in Fig. 3a) and a uniform, fast velocity in the shallow faceted prism (depicted as red in Fig. 3a). This ideal design has a shallow section of 5-μm depth and deep inlet and outlet sections of 50-μm depth. Since the speeds in the shallow and deep sections are related by continuity,[6, 7] the speed in the shallow section is 10 times that of the deep sections. The corresponding experimentally measured velocity field is shown in Fig. 3b (the microscope objective was centered over the right hand side of the facet of Fig.3a). Here, the speed fields in both deep and shallow sections are found to be substantially uniform, with the fluid moving quickly in the shallow faceted prism (red) and slowly in the deep channel section (blue). The ratio of average velocity (averaging the velocity along a line across the channel, normal to the side-walls) in the shallow facet to that in the deep section is 16:1. Part of this discrepancy results from a mask offset in which the deep section is 20% too wide (when compared to the ideal channel of Fig. 3a). Correcting for this offset using continuity, the resulting effective velocity ratio becomes 13:1, which remains larger than the ideal ratio. This deviation from design dimensions arises from errors in the etch time and sagging of the channel roof during the thermal bonding process. The spatial near-uniformity of the experimental PIV result in both the deep channel and the shallow region indicates that the deviation from ideal behavior in the straight channel geometry is minimal, and is limited to the relative magnitudes of the fluid flow in the shallow and deep channel sections.

The simulation of the as-fabricated straight channel geometry (Fig. 3c) is qualitatively the same as the experimental velocity field (Fig. 3b) and also shows that the etch effect on the velocity field is small, as seen by comparison to the designed channel simulation (Fig. 3a). The small gradient at the facet corners in the experimental velocity field is anticipated by the as-fabricated simulation due to the change in cross-sectional area that occurs upon entering and leaving the facet. In the as-designed case, the velocity change is spatially abrupt at the interface due to the constant channel width and the channel walls and floor being perpendicular (Fig. 2c, left), while the as-fabricated simulation shows a spatial gradient in the velocity field. This gradient extends 45 μm (the length of the isotropic-etch wall-arc – corresponding to $(d_1 - d_2)$ in Fig. 2c, right) away from the facet.

1.3.2 Displacer Channel

A displacer element translates a channel perpendicular to the direction of fluid flow, with the input and output flows traveling parallel to one another (Fig. 1 a, b). It forms the base element for faceted-prism turns and expanders.[6, 7] It also represents the primary element for insulating-ridge devices based on faceted prisms that perform particle filtration and concentration using dielectrophoresis.[25] The velocity field of a displacer element, designed using the spatially-uniform, faceted-prism approach, is shown in Fig. 4a. The slight speed field variation indicated by the color variation along the facet-sidewall connection (red, highlighted by arrow) is caused by the finite numerical resolution of the simulation, as is the minor, saw-tooth color variation (darker blue) at the facet-channel interface.

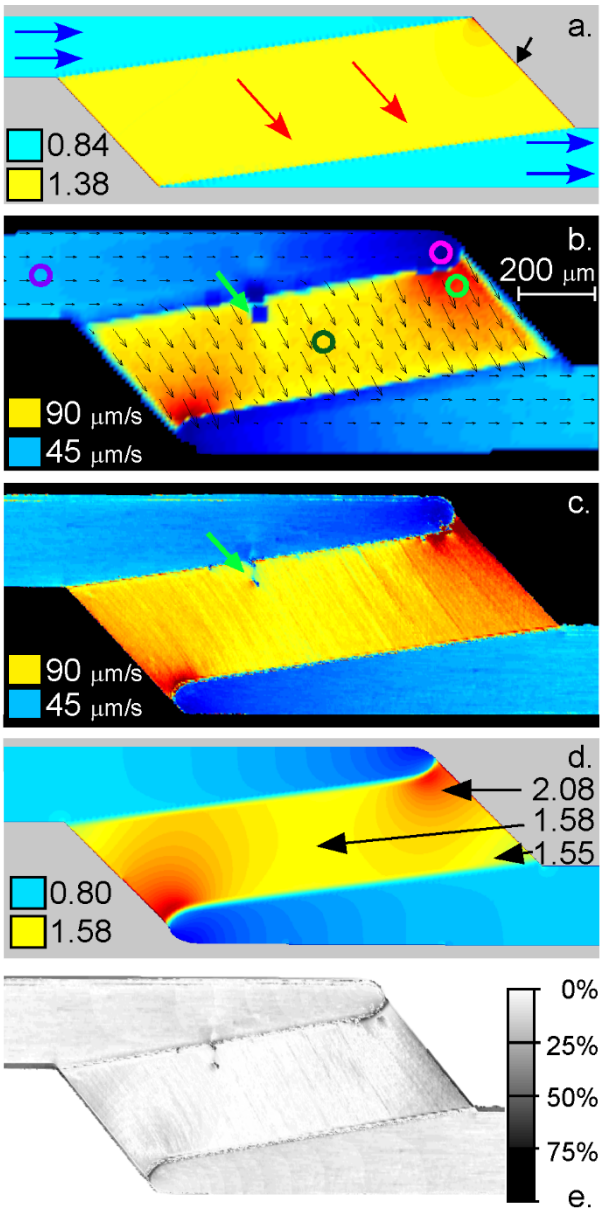

Figure 4. a. Laplace simulation of the as-designed displacer-channel velocity field. The ratio of deep channel to ridge fluid depths in the simulation is 10:1. The blue and red arrows indicate the flow directions; the small black arrow highlights the red pixels that are an artifact of the numerical simulation grid. b. Experimental PIV velocity field using 16x16 pixel resolution of the 50:5 μm displacer channel. The green arrow highlights a particle aggregate that has become lodged in the facet. The velocity in the magenta circle is 8% of that in the purple circle; the velocity in the light green circle is 33% greater then that in the dark green circle. c. Experimental PIV velocity field of the 50:5 μm displacer channel using single pixel resolution. The same data set was used for Fig. 4b and 4c. d. Laplace simulation of the as-fabricated displacer channel velocity field. The simulation velocities are in arbitrary units. e. Difference map of the experimental (Fig. 4c) and simulated (Fig. 4d) velocity fields.

The corresponding experimental electrokinetic velocity field in the displacer channel (Fig. 4b) is largely uniform. The two regions that deviate from this behavior are found in the rounded corners generated by wet-etch channel fabrication (top-right and bottom-left of the channel) and the adjacent region in the facet. The same behavior is observed in the symmetry-related exit to the facet (bottom-left of the facet in Fig. 4b). The slow speed in the acute corner of the deep channel (magenta circle in Fig. 4b) is 8% of that in the middle of the inlet (purple circle in Fig. 4b), while the adjacent fast speed at the edge of the facet is 33% greater than that in the center of the facet (light green and dark green circles in Fig. 4b, respectively).

To explore further the observed field variations and the slow velocity in one interrogation box (which appears as a square blue box in the low-resolution data analysis of Fig. 4b and is due to a lodged bead agglomeration), the PIV analysis was repeated using the single-pixel analysis code. As shown in Fig. 4c, high resolution analysis identifies the same variations in the velocity field across the faceted prism and indicates that the use of a larger interrogation box reliably represents the channel's velocity field. Single-pixel analysis shows that the flow non-uniformity about the lodged agglomeration of particles is limited spatially to the particle location, as indicated by the green arrow of Fig. 4c, where the spatial

extent of the disturbance is ~230 μm^2. Additionally, use of the single-pixel code allows fields to be interrogated immediately adjacent to the faceted interfaces where manufacturing anomalies (such as cracks or roughness in the facet face) can occur. The anomalous alternating yellow and orange streaks that appear in the field for the shallow, faceted prism of Fig. 4c are an artifact of the analysis code, which weights the integrated fluorescence intensity of large particle agglomerates more than that for individual beads. Because the lower resolution software is sufficient to interrogate the fields for the present study, and because of the prohibitive run time required to use the code, we avoid using data for which polystyrene particles lodge in channels at substantial levels. Such channel fouling becomes more prevalent as a given micro channel undergoes repeated use, requiring the use of a fresh channel for the present studies. Having obtained the field variation experimentally, the 2D Laplace solver was used to simulate the velocity field of the as-fabricated displacer channel, resulting in the velocity field shown in Fig. 4d. The field distribution obtained using the simulation is similar to the experimental fields of Figs. 4b and 4c. The fluid speed in the facet varies by 32% between the middle of the facet and the faster region in the corner (Fig. 4d), while the experimental speed difference between these two points (green circles in Fig. 4b) is 33%. This agreement is reinforced by the image of Fig. 4e, which represents a difference map between Fig. 4c and Fig. 4d, after normalizing the relative field magnitudes. As shown, the local difference between the experimental and numerical relative speed-field maps is less than 5%. This observation shows that deviations from ideal design caused by manufacturing limitations can be accounted for in future designs by application of 2D simulations of physically relevant channel geometries.

1.3.3 Splitter Channel

Flow splitters are useful for performing multiple, parallel analyses on a single chip. Faceted prism designs can also be useful for constructing flow splitters capable of dividing an inlet flow into any number of outlet flows, while retaining spatially-uniform field distributions.[6] Alternatively, faceted flow splitters can be operated in reverse to function as flow combiners. [7] When splitters and combiners are placed in sequence, they can be used to form benign channel supports within a wide microchannel.[6] Therefore, we have also examined the operation of a simple, 2-way splitter (Fig. 5). The electrokinetic speed field of an ideal flow splitter is shown in Fig. 5a, displaying a uniform velocity in the deep channels (blue) and a faster, uniform velocity in the shallow, faceted prisms (red). The experimental velocity field is shown in Fig. 5b. Here, the speed field in the top facet of the splitter is observed to be less than that in the lower facet by ~15%. This difference is consistent with a different depth in the two channels resulting from variability in etching within channels as a function of position across the substrate.

The simulated as-fabricated splitter channel velocity field with the same ridge depths in each shallow, faceted-prism predicts a symmetric flow field, (Fig. 5c) consistent with the above explanation. The deviation from spatial uniformity predicted for the splitter channel – the fluid velocity varies by 10% across the facet (Fig. 5c) – is much less pronounced than for the displacer channel (30% variation as indicated in Fig. 4d). This observation indicates that the variation in fluid speed depends not only upon the fabrication method, but also upon the specific channel geometry.

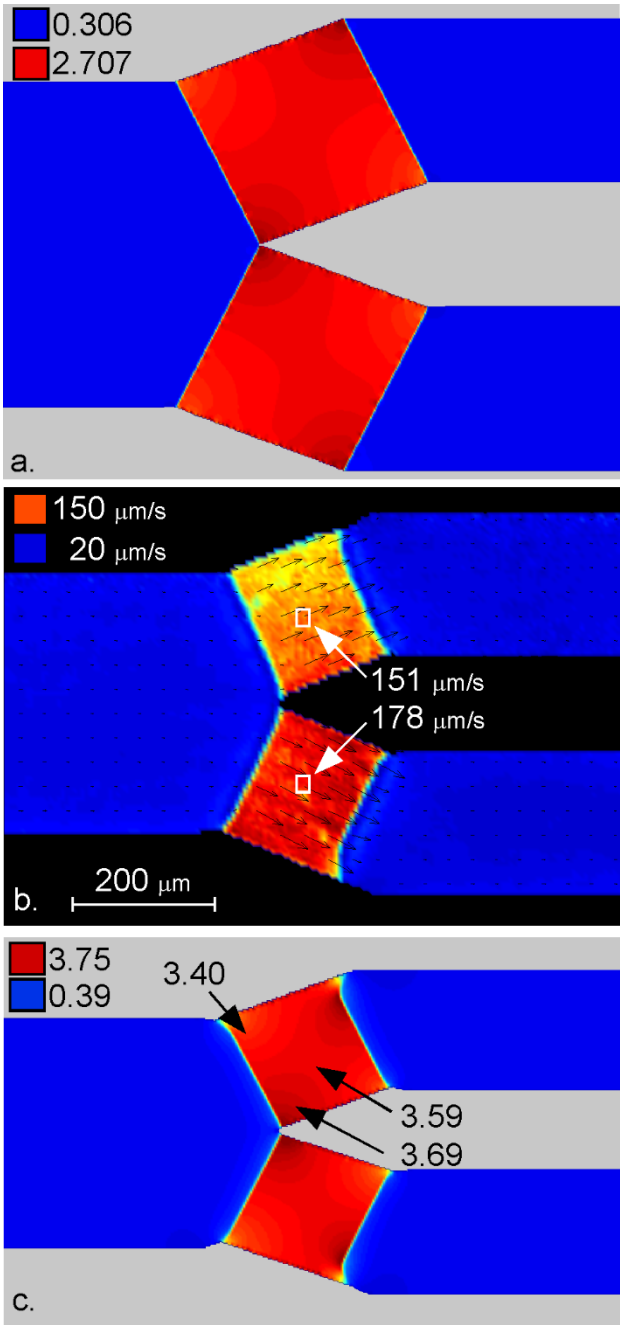

Figure 5. a. Laplace simulation of the as-designed splitter channel velocity field. The ratio of deep channel to ridge fluid depths in the simulation is 10:1. b. Experimental PIV velocity field using 16x16 pixel resolution of the 50:5 µm splitter channel. c. Laplace simulation of the as-fabricated displacer channel velocity field. The simulation velocities are in arbitrary units.

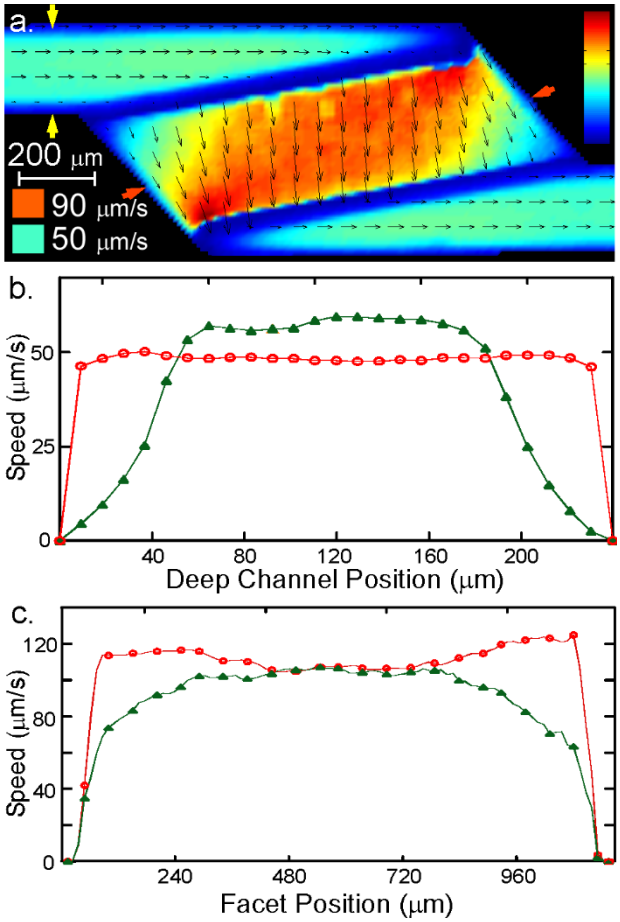

Figure 6. a. PIV-derived hydrodynamic flow field of the displacer channel. b, c. Cross sectional speed profiles for electrokinetic (red) and pressure-driven (green) flow in the displacer channel geometry at two locations. The line joining the yellow arrows in (a) indicates where deep channel speed profiles shown in (b) were obtained. The line joining the orange arrows in (a) indicates where the shallow channel speed profiles shown in (c) were measured.

1.3.4 Pressure-driven flow

The speed field of a pressure-driven flow through the displacer channel is shown in Fig. 6a. For these pressure-driven flow experiments, the Reynolds number is below 0.01, such that flow is always laminar. The resulting flow field displays significant differences in comparison to the corresponding electrokinetic flow field (Fig. 4b). During pressure-driven flow, the velocity across the channel (perpendicular to the flow direction) varies, with the speed at the center of the channel greater than that near the walls. This is caused by the influence of drag at the walls of the channel,[55] and the large surface-to-volume ratio of the present designs. This behavior is also observed in the shallow, faceted prism, with the middle of the channel exhibiting a greater speed than at the side walls.

The cross-sectional speed profiles of the electrokinetic vs. pressure-driven flows were investigated in both the deep channel (line joining yellow arrows in Fig. 6a, speed profile shown in Fig. 6b) and the facet (line joining orange arrows in Fig. 6a, speed profile shown in Fig. 6c). The deep-channel electrokinetic flow is comparatively uniform, rapidly decreasing to zero within 5 μm of the sidewalls, well within the 50 μm etch radius. In contrast, the deep-channel pressure-driven speed field increases more slowly with increasing distance from the side walls, before leveling off 75 μm from the walls. The cross-sectional electrokinetic speed field for the shallow, faceted prism is relatively less uniform than in the channel, displaying a slight dip in speed in the middle of the channel that is 18% lower than

the maximum speed. Nevertheless, the electrokinetic flow profile remains quite flat, particularly when compared to the superimposed pressure-driven profile. This pressure-driven local variation in speed along a faceted interface could cause leakage of particles for a filter/concentrator where the design requires spatially-uniform forces, and is to be minimized accordingly.

1.4 Discussion

The presence of the rounded corners caused by an isotropic etch fabrication method has been observed to lead to spatial variation in the velocity fields of three channel designs; straight, displacer and splitter. The variation increased with incidence angle of the faceted interface; it was smallest for the straight channel where the facet face is normal to flow and greatest for the displacer channel which had the largest incident angle of the three. Therefore, the fabrication method will place an upper bound on the incidence angle that can be employed for a device with a given tolerance for velocity variation.

Simulations were repeated to explore the magnitude of the etch effect on the cross-channel velocity profile. As the displacer channel velocity field was the most sensitive to isotropic etching of the three geometries presented, this channel was chosen as a test geometry. Fig. 7a shows the change in channel geometry with an increase in the etch depth. The greyscaled background is the as-designed geometry, the red, dashed line has an etch depth that is 9% of the displacer inlet channel width, while this value is 21% for the green, dashed line. The resulting cross-facet velocity profiles (corresponding to the line joining the orange arrows in Fig. 6a) show faster speed near the walls and a slower speed in the middle (Fig. 7b). This is consistent with the results of the μPIV experiments (Fig. 6c). The shape of the velocity profile curves is quite similar for all curves except for the 21% etch:deep channel ratio whose maximum closer to the center of the channel than the other etch depths. This results from an etch depth that approaches the magnitude of the channel width. The percentage variation in the velocity field across the channel increases linearly with etch depth for small etch depths, and the gradient decreases for larger etch depths (Fig. 7c) as the deviation from the ideal geometry becomes greater. The linear increase in simulated cross-facet velocity variation for small etch depths indicates that there is no threshold depth above which cross-facet velocity variations suddenly become prevalent and that should not be crossed when designing a spatially-uniform electrokinetic flow channel.

Using such calculations, it is possible to estimate the tolerable etch depth with respect to the channel width based on relative deviation from velocity-field uniformity for a given location within a channel. For a device in which a 15% deviation of cross-facet velocity is acceptable (~±7.5% from the mean), the maximum etch depth is 12% of the channel width (illustrated by the red dashed lines in Fig. 7c). Thus, if a channel width of 100 μm is required, the etch depth must be 12 μm or less. Conversely, to redesign the displacer channel to have a cross-facet velocity variation of less than 5% (blue dashed lines in Fig. 7c), with a facet depth of 5 μm and a 50-μm-deep channel depth, the maximum etch depth is 3% of the channel width, requiring 1725-μm-wide inlet and outlet channels.

The general channel design paradigm for minimizing spatial variation in the velocity field of channels constructed using the faceted prism approach is to minimize the ratio of the etch depth to channel width. This can be achieved by a combination of decreasing the etch depth, resulting in a smaller channel cross-sectional area, and increasing the channel width. The preferred magnitudes of these two parameters vary with the intended application and depend on the required fluid throughput, the size of species present in the fluid and fabrication limitations.

The implications for separations applications are clear: dispersion leads to analyte band broadening, lowering the resolution and detection limit of the device. Skew-induced dispersion can be minimized using uniform-field design. For particle filtration applications using IDEP, the uniformity of velocity fields allows more precise balancing of electrokinetic and dielectrophoretic forces on particles across

the entire length of an insulating ridge. This permits more sensitive tuning of device performance to allow the device to be used to separate mixtures of analytes.

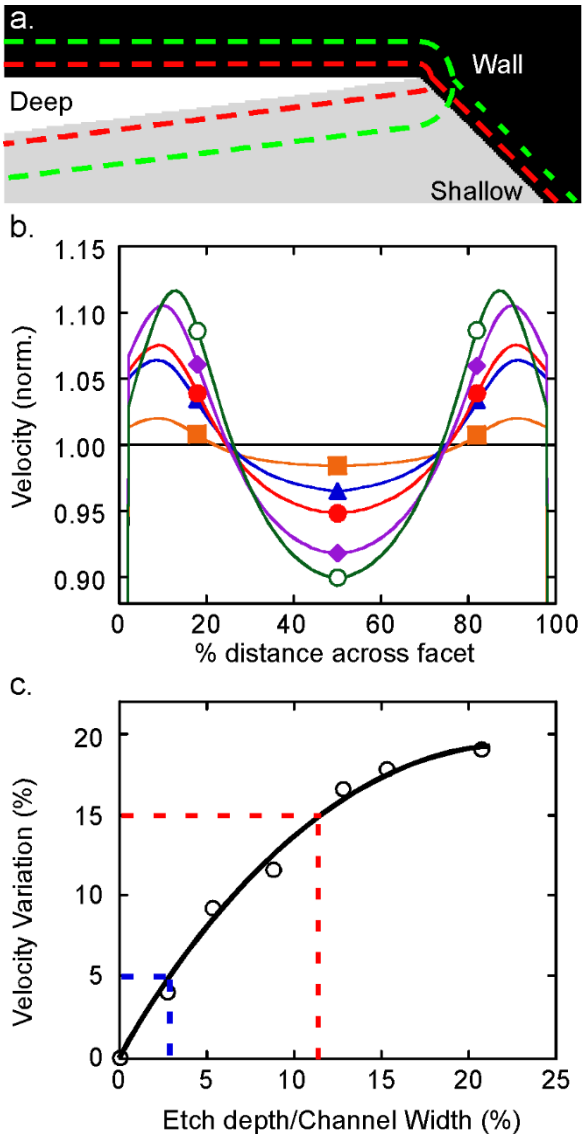

Figure 7. a. Change in channel shape in the corner of the displacer channel with increasing etch depth. For the green dashed line the etch depth is 21% of the inlet channel width and the red dashed line is 9%. This is superimposed on the as-designed displacer channel geometry. b. Fluid velocity across the middle of the facet in the displacer channel (the same line as denoted by the orange arrows in Fig. 6a). Each line is the etch depth as a percentage of the deep-inlet channel width; 3% (orange/square), 5% (blue/triangle), 9% (red/circle), 13% (purple/diamond), 21% (green/open circle). All velocities have been normalized to the same net flow through the facet. The three trace markers (open circle, etc) for each line are included to aid comprehension. c. Etch depth as a percentage of the inlet channel width vs. percentage cross-facet velocity variation. The data points are the percentage difference between the maximum and minimum of the simulated velocity profiles shown in 7b (this excludes the zero velocity at the walls). The black line is a generic smooth fitting curve included for clarity. The dashed red line illustrates the maximum etch depth:channel depth ratio for a channel with 15% cross-facet velocity variation, while the dashed blue line corresponds to a 5% variation.

1.5 Conclusions

The present study represents the first quantitative experimental study of field uniformity for the faceted-prism technique. The rational design and fabrication of controlled, ideal electrokinetic devices has been demonstrated for several geometries. The resulting experimental electrokinetic velocity fields have been quantitatively compared with the predictions of simple theoretical models. From this study, we conclude:

1. Deviations from exact mathematical designs result in velocity-field nonuniformity. In the case of isotropic etching, designs cannot be reproduced directly.
2. The resulting channels can be modeled reliably using simple, 2-dimensional simulations. These simulations can be extended to estimate minimum channel depths or widths necessary to minimize field variation across faceted prisms.

3. Pressure-driven flow, which cannot be simulated using the techniques shown in this manuscript, results in flow-field nonuniformity that is comparatively large, and is to be minimized.

Two-dimensional simulation of channel geometries using ideal electrokinetic theory is a powerful tool for the rational design and optimization of electrokinetically-driven microfluidic devices. When this approach is combined with experimental testing of theoretical predictions, and integrated into the development phase, the resulting devices performance promises to be greatly enhanced. A device based on such design is presented in a second paper, in which we demonstrate the filtration/concentration of particles.[25]

1.6 References

(1) Ehrfeld, W.; Hessel, V.; Lowe, H. *Microreactors: New Technology for Modern Chemistry*; Wiley-VCH: Weinheim, 2000.
(2) Andersson, H.; van den Berg, A. *Sensors and Actuators B: Chemical* **2003**, *92*, 315-325.
(3) Kikutani, Y.; Hibara, A.; Uchiyama, K.; Hisamoto, H.; Tokeshi, M.; Kitamori, T. *Lab On A Chip* **2002**, *2*, 193-196.
(4) Kikutani, Y.; Hisamoto, H.; Tokeshi, M.; Kitamori, T. *Lab On A Chip* **2004**, *4*, 328-332.
(5) Paegel, B. M.; Emrich, C. A.; Weyemayer, G. J.; Scherer, J. R.; Mathies, R. A. *Proc. Natl. Acad. Sci. U. S. A.* **2002**, *99*, 574-579.
(6) Fiechtner, G. J.; Cummings, E. B. *J. Chrom. A* **2004**, *1027*, 245-257.
(7) Fiechtner, G. J.; Cummings, E. B. *Anal. Chem.* **2003**, *75*, 4747-4755.
(8) Zubritsky, E. *Anal. Chem.* **2000**, *72*, 687A-690A.
(9) Paegel, B. M.; Hutt, L. D.; Simpson, P. C.; Mathies, R. A. *Anal. Chem.* **2000**, *72*, 3030-3037.
(10) Petersen, N. J.; Mogensen, K. B.; Kutter, J. P. *Electrophoresis* **2002**, *23*, 3528-3536.
(11) Mogensen, K. B.; Petersen, N. J.; Hubner, J.; Kutter, J. P. *Electrophoresis* **2001**, *22*, 3930-3938.
(12) Molho, J. I.; Herr, A. E.; Mosier, B. P.; Santiago, J. G.; Kenny, T. W.; Brennen, R. A.; Gordon, G. B.; Mohammadi, B. *Anal. Chem.* **2001**, *73*, 1350-1360.
(13) Griffiths, S. K.; Nilson, R. H. *Anal. Chem.* **2001**, *73*, 272-278.
(14) Culbertson, C. T.; Jacobson, S. C.; Ramsey, J. M. *Anal. Chem.* **1998**, *70*, 3781-3789.
(15) Griffiths, S. K.; Nilson, R. H. *Anal. Chem.* **2002**, *74*, 2960-2967.
(16) Culbertson, C. T.; Jacobson, S. C.; Ramsey, J. M. *Anal. Chem.* **2000**, *72*, 5814-5819.
(17) Johnson, T. J.; Ross, D.; Gaitan, M.; Locascio, L. E. *Anal. Chem.* **2001**, *73*, 3656-3661.
(18) Dutta, D.; Leighton, D. T. *Anal. Chem.* **2002**, *74*, 1007-1016.
(19) Benguigui, L.; Lin, I. J. *J. Appl. Phys.* **1984**, *56*, 3294-3297.
(20) Shediac, R.; Ngola, S. M.; Throckmorton, D. J.; Anex, D. S.; Shepodd, T. J.; Singh, A. K. *J. Chromatogr. A* **2001**, *925*, 251-263.
(21) West, J. A. A.; Hukari, K. W.; Shepodd, T. J.; Hux, G. J., 8th International Conference on Miniturized Systems in Chemistry and Life Sciences, Malmo, Sweden 2001; Royal Society of Chemistry; 656-658.
(22) Cummings, E.; Singh, A. *Anal. Chem.* **2003**, *75*, 4724-4731.
(23) Lapizco-Encinas, B. H.; Simmons, B. A.; Cummings, E. B.; Fintschenko, Y. *Anal. Chem.* **2004**, *76*, 1571-1579.
(24) Lapizco-Encinas, B. H.; Simmons, B. A.; Cummings, E. B.; Fintschenko, Y. *Electrophoresis* **2004**, *25*, 1695-1704.
(25) Barrett, L. M.; Skulan, A. J.; Singh, A. K.; Cummings, E. B.; Fiechtner, G. J. *Anal. Chem.* **2005**, *submitted*.
(26) Bruin, G. J. M. *Electrophoresis* **2000**, *21*, 3931-3951.
(27) West, J. A. A.; Lane, T. W.; Stamps, J. F.; Shokair, I. R.; Freutel, J. A., 7th International Conference on Micro Total Analysis Systems, Squaw Valley, USA 2003; MESA Monographs; 143-146.
(28) Jacobson, S. C.; Hergenroder, R.; Moore, A. W.; Ramsey, J. M. *Anal. Chem.* **1994**, *66*, 4127-4132.
(29) Liu, R. H.; Stremler, M. A.; Sharp, K. V.; Olsen, M. G.; Santiago, J. G.; Adrian, R. J.; Aref, H.; Beebe, D. J. *Journal of Microelectromechanical Systems* **2000**, *9*, 190-197.
(30) Roulet, J. C.; Volkel, R.; Herzig, H. P.; Verpoorte, E.; de Rooij, N. F.; Dandliker, R. *Anal. Chem.* **2002**, *74*, 3400-3407.
(31) Roberts, M. A.; Rossier, J. S.; Bercier, P.; Girault, H. *Anal. Chem.* **1997**, *69*, 2035-2042.
(32) Rossier, J.; Reymond, F.; Michel, P. E. *Electrophoresis* **2002**, *23*, 858-867.
(33) Johnson, T. J.; Waddell, E. A.; Kramer, G. W.; Locascio, L. E. *Appl. Surf. Sci.* **2001**, *181*, 149-159.
(34) Gerlach, A.; Knebel, G.; Guber, A. E.; Heckele, M.; Herrmann, D.; Muslija, A.; Schaller, T. *Sens. Mater. (Japan)* **2002**, *14*, 119-128.
(35) Chen, Z. F.; Gao, Y. H.; Lin, J. M.; Su, R. G.; Xie, Y. *J. Chromatogr. A* **2004**, *1038*, 239-245.
(36) Becker, H.; Heim, U. *Sens. Mater. (Japan)* **1999**, *11*, 297-304.
(37) McCormick, R. M.; Nelson, R. J.; AlonsoAmigo, M. G.; Benvegnu, J.; Hooper, H. H. *Anal. Chem.* **1997**, *69*, 2626-2630.
(38) Edwards, T. L.; Mohanty, S. K.; Edwards, R. K.; Thomas, C. L.; Frazier, A. B. *Sens. Mater. (Japan)* **2002**, *14*, 167-178.
(39) Hulme, J. P.; Mohr, S.; Goddard, N. J.; Fielden, P. R. *Lab On A Chip* **2002**, *2*, 203-206.
(40) Fan, Z. H.; Harrison, D. J. *Anal. Chem.* **1994**, *66*, 177-184.
(41) Fister, J. C.; Jacobson, S. C.; Davis, L. M.; Ramsey, J. M. *Anal. Chem.* **1998**, *70*, 431-437.
(42) Harrison, D. J.; Fluri, K.; Seiler, K.; Fan, Z. H.; Effenhauser, C. S.; Manz, A. *Science* **1993**, *261*, 895-897.
(43) Sun, K.; Yamaguchi, A.; Ishida, Y.; Matsuo, S.; Misawa, H. *Sensors and Actuators, B: Chemical* **2002**, *84*, 283-289.
(44) Madou, M. *Fundamentals of Microfabrication*; CRC Press LLC: Boca Raton, 1997.

(45) Santiago, J. G.; Wereley, S. T.; Meinhart, C. D.; Beebe, D. J.; Adrian, R. J. *Experiments in Fluids* **1998**, *25*, 316-319.
(46) Devasenathipathy, S.; Santiago, J. G.; Wereley, S. T.; Meinhart, C. D.; Takehara, K. *Experiments in Fluids* **2003**, *34*, 504-514.
(47) Cummings, E. B. *Experiments in Fluids 3rd International Workshop on Particle Image Velocimetry 3rd International Workshop on Particle Image Velocimetry; September 16-18, 1999; Santa Barbara, CA* **2000**, *29*, S42-S50.
(48) Santiago, J. G. *Anal. Chem.* **2001**, *73*, 2353-2365.
(49) Herr, A. E.; Molho, J. I.; Santiago, J. G.; Mungal, M. G.; Kenny, T. W.; Garguilo, M. G. *Anal. Chem.* **2000**, *72*, 1053-1057.
(50) Patankar, N. A.; Hu, H. H. *Anal. Chem.* **1998**, *70*, 1870-1881.
(51) Meinhart, C. D.; Wereley, S. T.; Gray, M. H. B. *Meas. Sci. Technol.* **2000**, *11*, 809-814.
(52) Cummings, E. B.; Griffiths, S. K.; Nilson, R. H.; Sandia National Laboratories: Livermore, CA, 2001; Vol. SAND 2002-8018, pp 65-93.
(53) Cummings, E. B.; Griffiths, S. K.; Nilson, R. H.; Paul, P. H. *Anal. Chem.* **2000**, *72*, 2526-2532.
(54) MacInnes, J. M. *Chem. Eng. Sci.* **2002**, *57*, 4539-4558.
(55) Probstein, R. *Physicochemical Hydrodynamics*; John Wiley & Sons, Inc: New York, 1994.

This page intentionally left blank.

CHAPTER 2

2.1 Chapter 2 Introduction

New and improved techniques to characterize and sort microscopic sized particles and cells are in high demand for a wide range of applications in areas such as biomedical research, clinical diagnostics, and environmental analysis. During sample preparation, trapping of particles facilitates automation of labor intensive procedures such as filtration, washing and labeling. During sample analysis, the ability to direct particles selectively down a specific channel to an appropriate assay is useful. Also during analysis, trapping of particles in specific regions of a chip concentrates the particles, potentially enhancing reaction times, reducing reagent volumes, and improving detection limits. Having the ability to support both sample preparation and analysis, dielectrophoresis (DEP)[1] is an effective way to trap, manipulate, and separate a variety of particles such as ores,[2] clays,[3] bacteria,[4, 5] yeast cells,[6, 7] large DNA strands,[8] mammalian cells,[9, 10] blood cells,[10-12] cancer cells,[12-17]malaria-infected blood cells,[18, 19]CD 34 stem cells,[20, 21]dead cells,[22] viruses,[23, 24] and latex particles.[25-27]

DEP is the movement of polarizable and conductive particles toward or away from regions of high electric-field intensity in non-uniform electric fields.[27] When particles approach a field gradient, they experience a selective force owing to DEP which is proportional to the particle volume and the difference in complex conductivity of the particle and the fluid.[28] Depending on the relative magnitude of the particle conductivity and that of the fluid, the DEP force can act to drive particles toward regions of either high electric field strength or low electric field strength – types of DEP termed positive and negative, respectively. The DEP force can be used to trap, deflect and manipulate cells and particles.

Most commonly, DEP is driven by electric field non-uniformities arising from multiple electrodes embedded throughout a fluidic system. Recently, insulator-based dielectrophoresis (IDEP) has shown great promise as an alternative approach to conventional DEP. In IDEP, insulating structures (i.e., packing material,[29-34] posts or ridges[35-38]) result in gradients in local electric field, which is imparted using electrodes located only at the channel inlet and channel outlet. If the applied field has a DC component, this field can also produce an electrokinetic flow through the channel. In early realizations of IDEP, then called "multigradient DEP"[39, 40], the space between electrodes was packed with insulating material such as glass beads[29, 30, 33, 34] and particles were dielectrophoretically trapped in regions between the beads. While the resulting early devices were simple to construct and operate, design methods were not employed to pattern local field gradients. The advent of planar micromanufacturing has enabled the rational design of insulating structures for IDEP and more recently, a single, isotropic etch was used to fabricate insulating structures in precise arrays of a chosen geometric design.[41-43] Here, the requisite field gradients for DEP result from such insulating structures and therefore the technique has been called "insulator-based"[36, 37] or "electrodeless"[35, 41] DEP. Transport in microchannels containing arrays of insulating obstacles has been modeled using a Laplace solver based on the theory of ideal electrokinetic flow.[42] Experimental demonstrations of system designs arising from such modeling included localized arrays of particle-trapping structures and/or rows of concentrated particle streams.[36, 37, 43] Selective concentration of particles, including polystyrene latex spheres[42], bacteria[36, 37] and DNA[35] has been shown using IDEP. Moreover, selective local concentration has been produced between combinations of samples, including different species of bacteria,[36] bacteria and latex polystyrene beads,[37] and viable and non-viable organisms.[37]

We report on an important extension of the IDEP technique in which generation of uniform field gradients spanning an entire channel width is achieved through the use of microfluidic channels having two distinct channel depths.[44-46] This work takes advantage of the flexibility afforded by a dual-depth glass etching technique to construct insulating ridges along which particles are deflected and/or trapped. For a ridge to function as a selective filter/concentrator, it is desirable to have uniform fields on both sides of the interface (the leading edge of the ridge) between deep and shallow regions. The result is a field gradient that is uniform along a line parallel to the interface. Consequently, the ridge deflects particles uniformly along its entire leading (or trailing) edge. Without a channel design that produces uniform fields on each side of the ridge, DEP-induced particle motion will also vary along the ridge, allowing particles which are deflected or trapped at one side of the microchannel to pass over the ridge unaffected at other locations within the microchannel. To this end, we employ faceted prisms to fabricate insulating ridges.[47, 48] The technique was introduced by Fiechtner and Cummings,[47] who derived the design rules theoretically that are necessary for the design of ideal prismatic sections. In a companion paper[49] we present the first experimental demonstration of faceted prism microchannels, in which fields are applied at low levels, and images of the resulting velocity fields are obtained using particle image velocimetry. In the present manuscript, we present the first demonstration of the faceted-prism methodology for particle filtration and concentration by dielectrophoresis at comparatively large applied fields. The resulting insulating ridges are fabricated in a glass microfluidic device, in which polystyrene carboxylate-modified particles are trapped and concentrated experimentally. Finally, a two-component mixture of particles and vegetative *Bacillus subtilis* are fractionated, demonstrating the ability of the IDEP system to concentrate bacteria quickly and selectively.

2.2 Experimental

2.2.1 Chip fabrication

The microfluidic chips were fabricated from D263 glass substrates (100-mm diameter, 1.1-mm thick, S. I. Howard Glass Company, Worcester, MA) using standard photolithography, wet etch, and bonding techniques. To fabricate the ridge structures, a two-step etch process was employed.[44-46] After completion of the initial etch step, the etch process was repeated using a different mask resulting in trenches having regions of two distinct depths. The mask for the second etch was aligned with the first etch through the use of a pair of alignment marks located near the outer edges of the wafer. The alignment marks on the mask were overlaid with those on the wafer using a MA-6 Karl Suss aligner. Lids were formed using the same glass material (D263 glass) as the etched substrate. Via access holes were drilled in the cover plate with diamond-tipped drill bits (Amplex, Worcester, MA). The etched wafer and drilled cover plate was cleaned with 4:1 H_2SO_4/H_2O_2 (100 °C). The machined cover plate was rinsed with 1% HF solution to inhibit crack propagation. The substrates were then immersed in a 40% NaOH solution at 80°C, rinsed in a cascade bath, spun dry, aligned for contact and thermally bonded by slowly ramping the temperature to 610°C for 5 hours in a nitrogen-purged programmable muffle furnace (model 48000, Thermolyne Dubuque, IA).

2.2.2 Cell preparation

Bacillus subtilis (strain ATCC #6633) was obtained from ATCC (Manassas, VA, USA) and grown in Luria-Bertani (LB) nutrient broth. Cultures were grown overnight at 37°C in an incubator to achieve saturation conditions. A 1:10 volumetric dilution of the cell culture was then allowed to grow in the LB liquid broth into late log phase to a cell concentration of 6 x 10^8 cells/ml, verified by OD measurements at 600 nm.[50] Cells were centrifuged at 5000 rpm for 120 minutes to eliminate the LB nutrient broth. The cells were resuspended in deionised (DI) water using a vortex mixer. The cells were then labeled

with Syto®11 (green) or Syto®17 (red) (Molecular Probes, Inc., Eugene, OR) For every milliliter of cell culture present in the vial containing the live cells, three microliters of the Syto® dye was added. The cells were then incubated at room temperature for 10 minutes, concentrated by centrifugation at 5000 rpm for 10 minutes, washed with DI water to remove any free dye, and resuspended in DI water to the desired final volume to reach the appropriate cell concentration (typically 6 x 10^8 cells/ml). The DI water employed had a conductivity of 10 μS/mm, pH 7.7 (adjusted using concentrated sodium hydroxide)(Millipore).

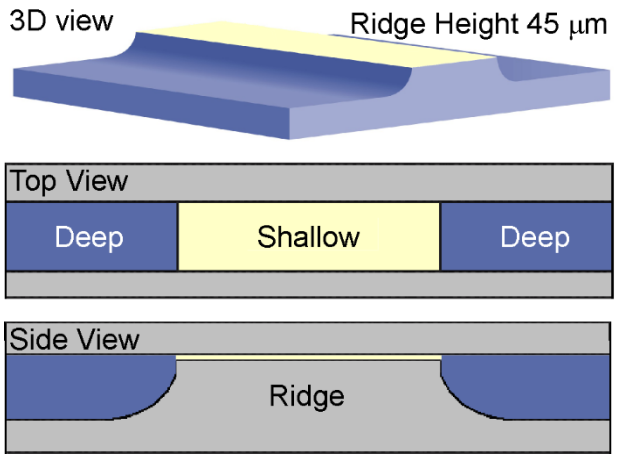

Fig 2.1: Schematic representations of an insulative ridge created using a two level isotropic etch of glass. The deep region (blue) is 50 μm deep, the shallow region (yellow) is 5 μm deep.

2.2.3 DEP Experiments

Pipette tips were used as fluid reservoirs and care was taken to minimize pressure-driven flow produced by liquid-level differences in the reservoirs before each run. A sample of labeled cells, inert polystyrene carboxylate-modified particles (Fluospheres, Molecular Probes, Eugene Oregon), hereafter referred to as 200-nm particles, or a mixture of both, were introduced at the inlet reservoir and outlet reservoir. Here the channels of the devices were filled with particles in absence of an applied field. Some particles can get lodged on the ridges during this filling stage—unwanted particle adhesion is often observed, becoming increasingly prevalent as a chip is reused from day-to-day. *Bacillus subtilis* can be washed from channels between experimental runs using surfactants, but this approach is less effective for the removal of polystyrene particles. Therefore, to minimize the influence of lodged particles, data is collected using fresh chips that are reused only a few times. Electrodes were placed at the inlet and outlet reservoir and an electric field was applied along the microchannel. The distance between the two electrodes was 10.2 mm. A high-voltage power supply (Stanford Research Systems, PS350, Palo Alto, CA) was used to apply electric fields by employing platinum-wire electrodes with a 0.5 mm diameter (Omega Engineering INC, Stamford, CT). Therefore, the reported field strengths (V/mm) represent nominal electric field strength, with the voltage applied along the entire 10.2-mm distance between electrodes. The behavior of the cells and inert particles was imaged using an inverted epi-fluorescence microscope (model IX-70, Olympus, Melville, NY) equipped with filter sets for dual-color imaging of red and green dyes (51006, Chroma Technologies Corp, Brattleboro, VT) and single-color imaging of green dye (Olympus U-MNB, Olympus, Melville, NY). Images were captured using a digital camera (Sony, San Diego, CA) and an image acquisition program (written in-hous

2.2.4 DEP Simulations

Simulations of the electrokinetic flow were performed using a previously reported electrokinetic and dielectrophoretic simulation code.[42, 51] These qualitative simulations elucidate how particles will behave in a device with regions of non-uniform field strengths under conditions where DEP is negligible and those where DEP is significant. For illustration purposes all the simulation diagrams follow a narrow band of particles and their relative positions at a certain point in time (tX). The numerical simulation approach solves the modified Laplace equation, $\sigma(x,y)\nabla\varphi(x,y) = 0$ for the electrostatic potential φ at each point in a two dimensional field σ that is proportional to the depth of the channel. The electrokinetic velocity of a particle is given by $u_{ek} = \mu_{ek} E$, where μ_{ek} is the electrokinetic mobility of the particle and E is the local electric field ($E = -\nabla\varphi(x,y)$). The dielectrophoretic velocity is $u_{dep} = \mu_{dep} \nabla(E\cdot E)$, where μ_{dep} is the dielectrophoretic mobility of the particle. Expressing the electrokinetic velocity as $\mu_{EK} \equiv \mu_{EP} - \mu_{EO}$, where μ_{EO} and μ_{EP} are the electroosmotic and electrophoretic mobility, respectively, we obtain the expression describing that, for deflection or trapping to occur,[36]

$$\frac{u_{DEP}\cdot u_{EK}}{u_{EK}\cdot u_{EK}} = \frac{\mu_{DEP}}{\left(\mu_{EP} - \mu_{EO}\right)}\frac{\nabla l}{l}\cdot E > 1 \qquad (1)$$

where $l \equiv \mathrm{E}\cdot\mathrm{E}$ is the local field intensity.

At low field strengths, the electrokinetic force component dominates, while at high field strengths the dielectrophoretic force component dominates in regions having local field gradients, such as at the interface between deep and shallow depth regions of a channel. For simplicity and clarity, the analysis presented here treats particles as infinitesimal points that are in local electrostatic equilibrium. The simulations neglect motion resulting explicitly from hydrodynamic lift and drag, buoyancy, finite polarization rate, and finite particle size effects.

2.3 Results and Discussion

A schematic representation of the insulating ridge geometry used in this work is shown in Fig. 2.1. Simulation results for a straight channel with a ridge oriented perpendicular to the flow direction are shown in Fig. 2.2.[49] This type of ridge represents the most trivial form of faceted prism, taken from a larger family of uniform-field designs.[47,48] The simulation was performed under conditions for which DEP is negligible (Fig. 2.2a) and also when DEP is significant (Fig. 2.2b). As can be observed in the simulation results, when DEP is insignificant (at low applied electric fields) the particles flow unhindered over the ridge.[49] Above a threshold applied electric field, which depends, in part, on the particle physical properties, DEP becomes appreciable and particles entering the system are inhibited from crossing the interface. Here, the value of this "inhibition threshold" depends on the ratio of the electrokinetic and dielectrophoretic particle mobility as governed by Eq. (1),[42] and the specific permeability ratio of the faceted-prism ridge, where, for example, an increase of the specific permeability ratio results in a larger field gradient between deep and shallow sections, such that $\mu_{dep}\nabla(E\cdot E)$ is correspondingly increased. The threshold value was examined experimentally for 200-nm particles, and the results are shown in Fig. 2.2c. Here, it is observed that when DEP is significant—in this case for an applied field strength of 100 V/mm or larger—trapping occurs along the leading interface of the ridge. A device such as this is useful for filtering and/or concentrating one type of particle from a sample of particles. Washing steps or labeling could be performed while the particles are trapped.

The device function is inherently altered by changing the incidence angle of the faceted prism (known as the interface angle for the ridge[47, 48]). This is illustrated by the vector diagrams of Fig. 2.3. The case for which θ=0 corresponds to a facet oriented perpendicular to the direction of flow, as was considered in Fig.2.2.

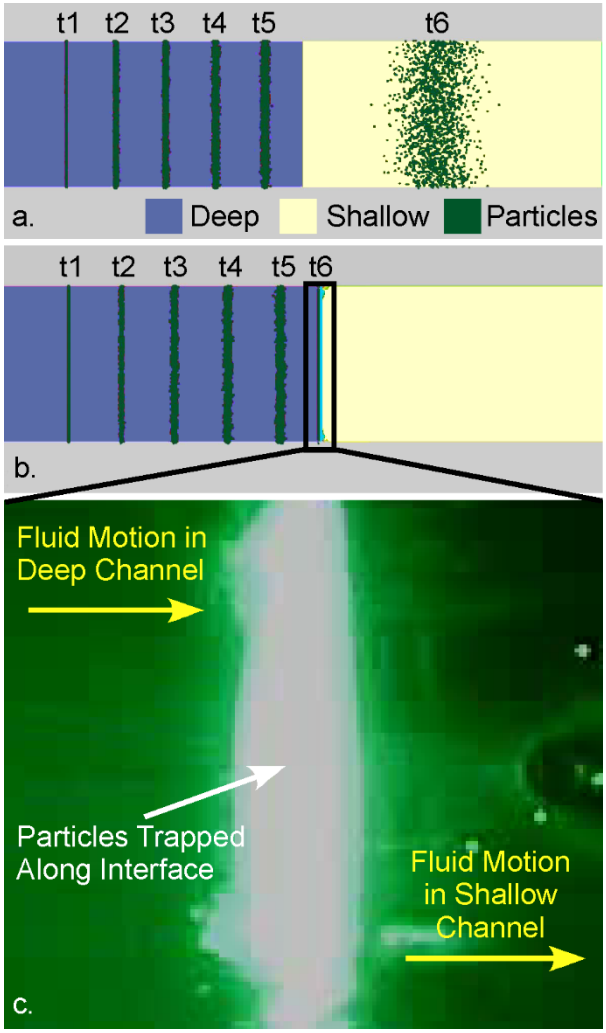

Fig. 2.2: Particle trapping at a ridge. (a) Simulation below DEP inhibition threshold, particles flow over the ridge. (b) Simulation above DEP inhibition threshold, particles trap just before the ridge. The deep region (blue) is 50 μm deep, the shallow region (yellow) is 5 μm deep. (c) Fluorescence image showing trapping of 200-nm particles at a ridge with an applied field strength of 100 V/mm.

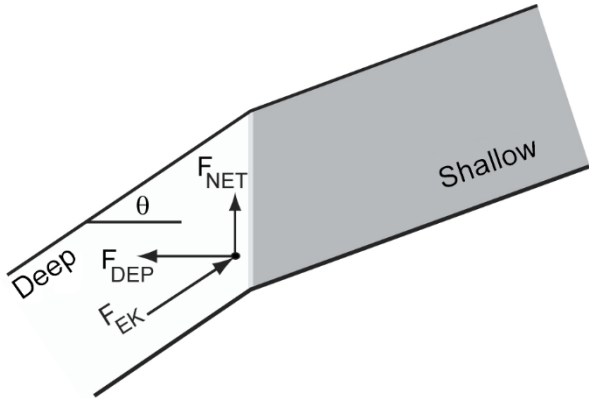

Fig.2.3: Vector diagram of the forces proportional to that caused by electrokinetic and dielectrophoretic effects, F_{EK} and F_{DEP}, respectively, for a particle near a faceted-prism interface. For nonzero interface angles, θ, the particle acquires a net motion parallel to the vector F_{NET}.

Here, the particles trap near the interface, where electrokinetic and dielectrophoretic forces balance. Alternatively, a faceted interface oriented at a nonzero angle θ with respect to the direction of flow allows the possibility of net motion, as is illustrated in the vector diagram of Fig. 2.3. Here, the field gradient, and hence, the direction that dielectrophoresis pushes the particles, no longer aligns with the incident electrokinetic field. The result is that particles are deflected along the ridge. This can be used, for example, to trap particles at a point (in contrast to trapping along a line, as is demonstrated in Fig. 2.2).

Alternatively, angled interfaces can be used to deflect particles continuously to a separate "concentration" channel. The faceted-prism methodology can be used to design a variety of micro channels, including flow splitters that divide an inlet channel into any number of outlet channels. Motivated by such faceted flow-splitter designs[48], a three-way flow splitter was designed and fabricated using the faceted-prism geometry shown in Fig. 2.4. Here, a single, 50-μm-deep inlet is split into three 50-μm-deep outlets. Two of the side channels have angled, faceted-prism ridges (45-μm high) at their entrances, while the center channel contains no faceted prism ridge. Figure 2.4c and 2.4d show simulation results for a single particle type migrating through the pitchfork geometry at applied field strengths below (Fig.2.4c) and above (Fig.2.4d) the inhibition threshold. In this case, the simulation includes effects such as etch-back that cause deviation from exact mathematical designs.[49] To demonstrate particle motion, bands of particles are superimposed on the flow inlet at time t1, and tracked through the channel for later instances t2-t5. As shown, particles flow exclusively out of the central channel when fields above the inhibition threshold are applied. For the present channel depths, the isotropic etching technique of channel fabrication causes deviations of channel geometry from ideal theory. Moreover, placement of the central channel also causes additional deviation from ideal designs. Nevertheless, the simulations show that above some threshold, particle deflection to the central channel should occur. Figure 2.5 shows the cross-facet values of E (black line) and $\nabla(E \cdot E)$ (red line), proportional to the electrokinetic and dielectrophoretic forces, F_{DEP} and F_{EK}, respectively, exerted on a particle. For DEP trapping or deflection to occur, F_{DEP} has to be greater than F_{EK} such that the conditions of Eq. (1) are satisfied.[36, 42]

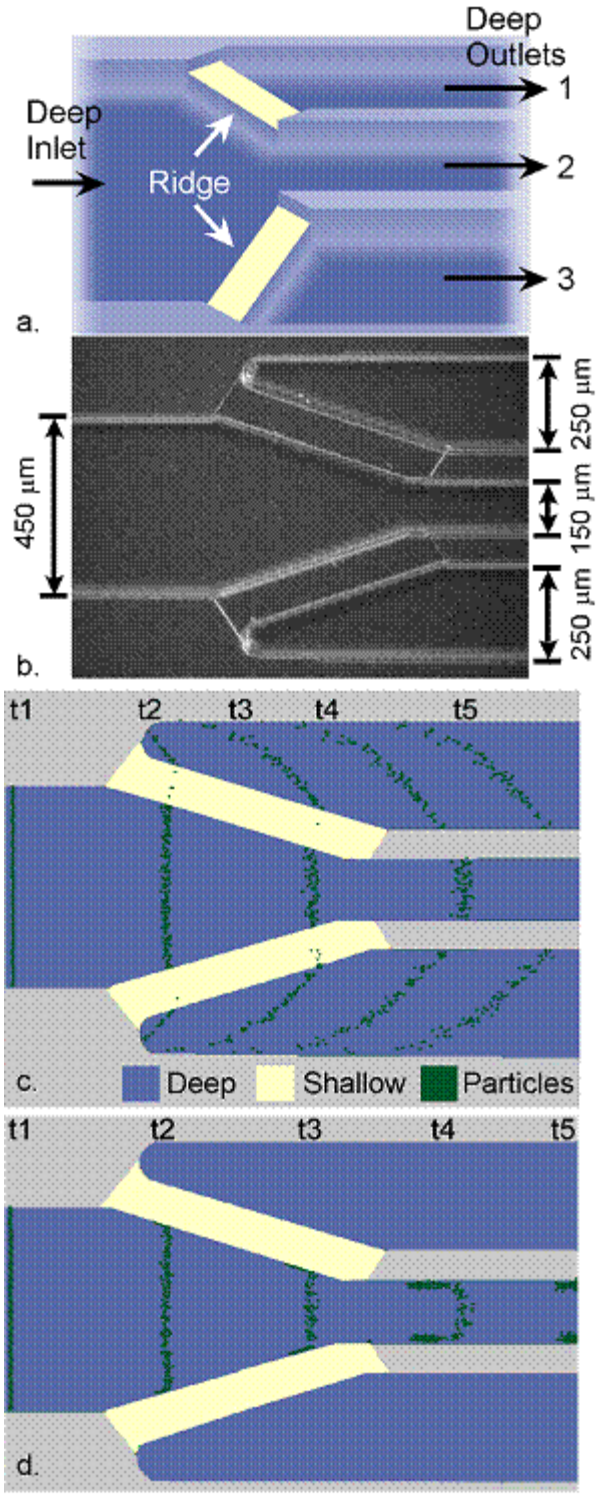

Fig. 2.4: Planar glass pitchfork channel geometry. (a) Schematic representation of two ridges in a channel with one inlet (left) and three outlets (right). (b) Micrograph of manufactured device. Length from inlet to outlet ports was 10.2 mm. (c) simulation below DEP threshold, particles flow over the insulative ridges and out through the three channels. (d) simulation above DEP threshold, particles are deflected by the insulative ridge and confined to the central channel. The deep region (blue) is 50 µm deep, the shallow region (yellow) is 5 µm deep. Flow is from left to right.

The simulations of Fig.2.4 identify significant band dispersion and bending in the central concentration channel. The amount of dispersion is larger when DEP is dominant (Fig.2.4d, t4) than for the low-field example of Fig. 2.4c. The larger dispersion when DEP is significant results from the deflection transit and delay that results for particles in the vicinity of an interface. If a sample was injected in a short window, as signified by line t1 in Fig.2.4d, then the resulting sample band that would arrive in the concentration channel at time t5 would be broadened by dispersion. This broader sample peak would require a wider temporal window when detecting with downstream analytical instruments.

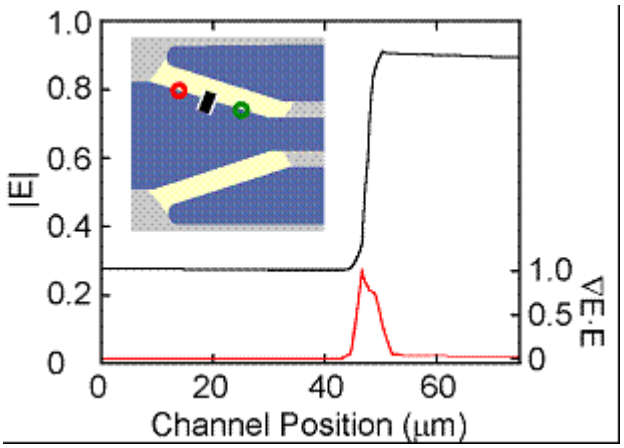

Fig. 2.5. Cross-facet electrokinetic (|E|, black line) and dielectrophoretic ($\nabla E \cdot E$, red line) magnitudes. The channel position corresponds to the black line on the inset picture of the pitchfork channel, with 0 μm in the inlet channel and 75 μm on the shallow facet. These data are derived from a Laplace simulation of the wet-etch geometry of the pitchfork channel. The scales are normalized to 1. The relative values of $\nabla E \cdot E$ at the three circles are: 1.29 (red circle) and 0.72 (green circle). $\nabla E \cdot E$ at the facet on the black line of the inset is normalized to 1.00.

However, an advantage of the pitchfork design is that samples can be concentrated continuously, minimizing the importance of such dispersion. In such a device, downstream diagnostics could be run continuously, collecting signal as concentrated sample flows by.

Samples of labeled *Bacillus subtilis*, 200-nm particles, and a mixture of both were introduced at the inlet reservoir of the pitchfork channel geometry. The applied potential was systematically chosen in an effort to determine the inhibition threshold field strength for *Bacillus subtilis*. Figure 2.6a shows *Bacillus subtilis* flowing unhindered down the three exit channels in experiments at applied fields up to 10 V/mm. Figure 2.6b shows that at and above an applied field of 30 V/mm the flow of *Bacillus subtilis* was restricted to the central channel as a result of DEP deflection by the insulating ridges. The observed behavior indicates an inhibition threshold voltage of 30 V/mm for *Bacillus subtilis* in this device. As the applied electric fields investigated were below the inhibition threshold for the 200-nm polystyrene particles, dielectrophoresis produced by the insulating ridges was negligible and the 200-nm particles flowed uninhibited down each of the three exit channels.

To show that *Bacillus subtilis* could be selectively concentrated and separated from a two-component mixture, *Bacillus subtilis* (6×10^7 cells/ml) and 200-nm particles (4.5×10^8 particles/ml) were mixed and introduced into the device. Upon application of fields up to 30 V/mm, both types of particles passed through the three exit channels. At 30 V/mm, the *Bacillus subtilis* flow was confined to the central channel while the 200-nm particles continued to flow freely through the three outlet channels, demonstrating the feasibility of IDEP as a sample concentrator and fractionation technique. Clearly visible over one of the faceted ridges in Fig. 6c is the adhesion of beads to the surface of the channel. This resulted when loading the channel during earlier experimental runs, and does not result from electrokinetic or dielectrophoretic effects. Such fouling is caused by sticking of polystyrene particles, and limits the number or useful runs for each channel to a few repeated cases.

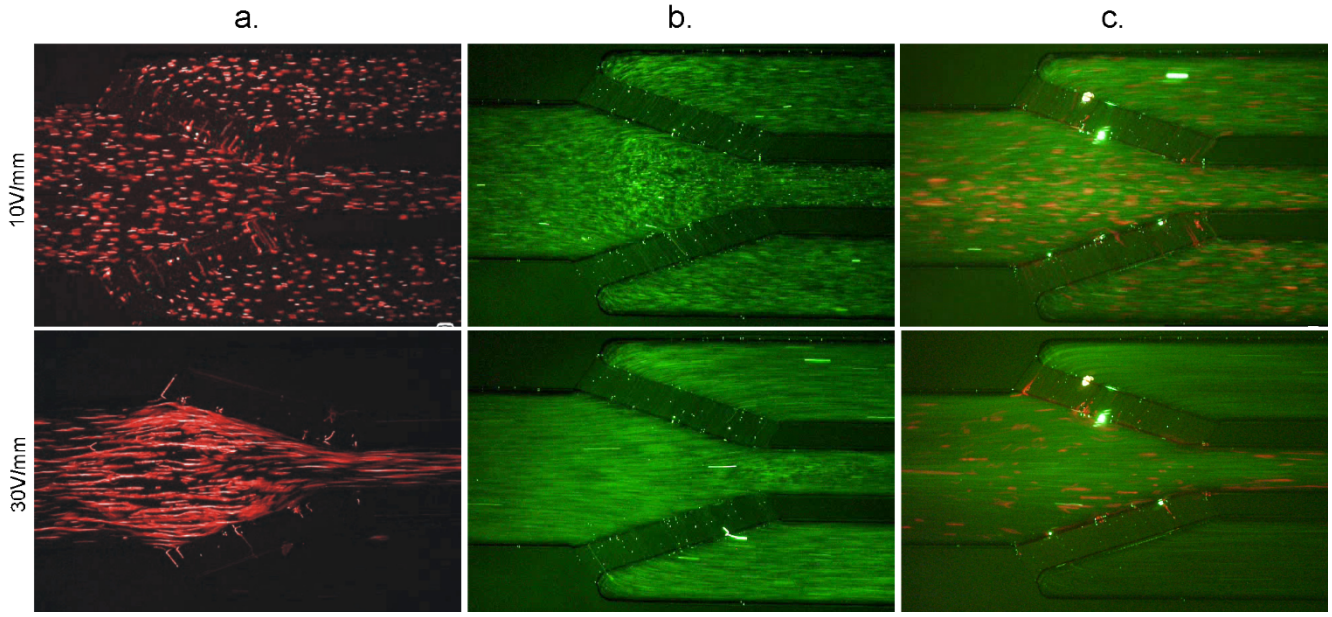

Fig 2.6. Particle-specific confinement using IDEP. Flow is from left to right a: *Bacillus subtilis* (6 x 10^6 cells/ml) confined by DEP to flow down only the center channel at E = 30 V/mm. Note that *Bacillus subtilis* shown here were labeled green (Syto® 11) but are falsely colored red for consistency. b: 200-nm particles (4.5 x 10^7 particles/ml) flowing freely through all three outlet channels, c: Two-component sample of *Bacillus subtilis* (6 x 10^7 cells/ml) and 200-nm particles (4.5 x 10^8 particles/ml).

Deviations from ideal channel design result in variations of patterned field gradients along ridge interfaces. In this case, the consequence is imperfect filter/concentrator operation, since the peak value of $\nabla(E\cdot E)$ is not uniform along the interface between deep and shallow sections. In the case of the pitchfork design shown in Fig.2.5, the peak value of $\nabla(E\cdot E)$ at the red and green circles is 129% and 72% of the value at the intersection of the black line with the facet-deep channel interface. This results in some sporadic leakage of *Bacillus subtilis* into the outer channels at threshold operation. This leakage occurs at the side walls of the ridge structures where there is curvature due to the isotropic etch. Although the rate of leakage is small, it indicates that the present designs could be improved. For example, recent experimental studies of the velocity fields in these channels have led to predictions for which the channel width and depth can be chosen for a deviation in field uniformity at a given location in the channel.[49] Future improvements will employ these design predictions to improve filter/concentrator operation.

The present data is limited to run times for which pressure buildup in the exit port is negligible. For longer runs, buildup of pressure head may cause unwanted effects from pressure effects on the behavior of the ridged concentrator. For example, back pressure can cause a change in the field distribution for faceted-prism design, as was demonstrated by Skulan and coworkers.[49] Consequently, the spatially nonuniform field distribution will likely cause particle leakage along the interface of faceted ridges. Back pressure will also introduce a pressure force on particles as they travel downstream, working largely against electrokinetic forces—this should result in lower threshold fields than normally observed. Pressure flow might also cause boundary-layer effects, where particles can leak near walls. If required, several methods could be used to minimize the influence of a buildup of pressure. For example, larger inlet and outlet reservoirs would reduce the buildup of pressure head differences as a function of time. In addition, channel coatings could be applied to reduce electroosmotic flow for a given applied field strength.

A number of examples have been published in recent years demonstrating the use of insulating structures incorporated into microchannels. For instance, numerous papers have been published[36, 37, 42] for which dielectrophoresis is demonstrated in an array of posts. These posts are constructed using a single etch, such that posts extend from the channel floor to the cover, and are, therefore, inherently easier to construct than the present two-level devices. For the post arrays, dielectrophoresis results from the squeezing of fields between rows of posts. In one past demonstration, *E. coli* is trapped at 200 V/mm while 200 nm beads flow freely through the array of posts. Therefore, the applied field magnitudes needed to affect cells by dielectrophoresis are generally larger than for the present study. Nevertheless, such a comparison is not trivial. For example, particles that are not trapped by the first row of posts can have their motion modified, which, in turn, impacts whether or not they trap at subsequent post rows. Moreover, particles that are trapped can then impact the trapping dynamics of particles that arrive at later times—an effect that can be substantial for comparatively large concentrations.

The function of post arrays is to trap particles at an array of locations within the channel. This inherently disperses filtered samples at many locations in a channel. Detection can then be achieved through techniques such as laser-induced fluorescence within an array, or, alternatively, the voltage can be dropped, releasing the particles for downstream diagnostics. This requires synchronization of the sample with downstream analytical instruments, and introduces the need to deal with sample dispersion from a sample that is distributed in an array. The use of ridges oriented perpendicular to the direction of flow (Fig. 2.2) also implements trap-and-release operation with detection along a line, or, similarly, sample can be released for downstream analytical detection. The amount of concentration can be increased by increasing the trapping time. The use of angled interfaces enables particle deflection, in which particles are selectively concentrated. This enables continuous operation, for which the concentration channel is monitored continuously by downstream analytical methods. The degree of concentration is determined by the splitter geometry, with the amount of concentration increasing as the width of the faceted-prism channels increases with respect to the width of the central concentration channel. Continuous concentration simplifies the synchronization of downstream analytical instruments with the dielectrophoretic concentrator, but replaces it with the need to match flow rates downstream.

2.4 Conclusions

We have presented the first demonstration of particle filtration and concentration using dielectrophresis with insulating ridges. Based on the faceted-prism methodology, these can be used to trap, deflect and concentrate particles selectively. Allowing both batch and continuous processing, these faceted geometries promise to facilitate the rational design of particle and cell manipulation devices for applications in sample preparation, analysis and detection. The devices presented were created using a two level etch process of an insulating substrate which produced channels having insulator based ridges. Conceptually, the ridge design of Fig. 2.2 can be employed to trap particles selectively in desired locations of a microchannel to support practical device functions. For example, particles can be detected directly at these locations or held in position for chemical reactions (i.e. labeling) or washing steps. Alternatively, particles can be released after a desired period of trapping/concentration for later batch processing. The device shown in Fig 2.5. demonstrates the potential use of IDEP in a continuous processing mode. This device could be used as is shown here to remove one particle type (*Bacillus subtilis*) from a multi component mixture. IDEP also has the ability to be used to deflect, continuously, particles down side channels for further processing.

2.5 References

(1) Gascoyne, P. R. C.; Vykoukal, J. *Electrophoresis* **2002**, *23*, 1973-1983.
(2) Lin, I. J.; Benguigui, L. *Separation and Purification Methods* **1981**, *10*, 53-72.
(3) Lockhart, N. C. *Powder Technology* **1983**, *35*, 17-22.
(4) Wang, X.-B.; Huang, Y.; Burt, J. P. H.; Markx, G. H.; Pethig, R. *Journal of Physics D: Applied Physics* **1993**, *26*, 1278-1285.
(5) Schnelle, T.; Muller, T.; Gradl, G.; Shirley, S. G.; Fuhr, G. *Journal of Electrostatics* **1999**, *47*, 121-132.
(6) Pethig, R.; Huang, Y.; Wang, X.-B.; Burt, J. P. H. *Journal of Physics D: Applied Physics* **1992**, *25*, 881-888.
(7) Markx, G. H.; Talary, M. S.; Pethig, R. *Journal of Biotechnology* **1994**, *32*, 29-37.
(8) Asbury, C. L.; Diercks, A. H.; Van den Engh, G. *Electrophoresis* **2002**, *23*, 2658-2666.
(9) Gascoyne, P. R. C.; Huang, Y.; Pethig, R.; Vykoukal, J.; Becker, F. F. *Measurement Science & Technology* **1992**, *3*, 439-445.
(10) Xu, C. X.; Wang, Y.; Cao, M.; Lu, Z. H. *Electrophoresis* **1999**, *20*, 1829-1831.
(11) Auerswald, J.; Knapp, H. F. *Microelectronic Engineering* **2003**, *67-68*, 879-886.
(12) Becker, F. F.; Wang, X.-B.; Huang, Y.; Pethig, R.; Vykoukal, J.; Gascoyne, P. R. C. *Journal of Physics D: Applied Physics* **1994**, *27*, 2659-2662.
(13) Becker, F. F.; Wang, X.-B.; Huang, Y.; Pethig, R.; Vykoukal, J.; Gascoyne, P. R. C. *Proc. Nat. Acad. Sci.* **1995**, *92*, 860-864.
(14) Gascoyne, P. R. C.; Wang, X. B.; Huang, Y.; Becker, F. F. *IEEE Transactions on Industry Applications* **1997**, *33*, 670-678.
(15) Cheng, J.; Sheldon, E. L.; Wu, L.; Heller, M. J.; O'Connell, J. P. *Analytical Chemistry* **1998**, *70*, 2321-2326.
(16) Burt, J. P. H.; Pethig, R.; Gascoyne, P. R. C.; Becker, F. F. *Biochimica et Biophysica Acta* **1990**, *1034*, 93-101.
(17) Gascoyne, P.; Pethig, R.; Satayavivad, J.; Becker, F. F.; Ruchirawat, M. *Biochimica et Biophysica Acta* **1997**, *1323*, 240-252.
(18) Gascoyne, P.; Mahidol, C.; Ruchirawat, M.; Satayavivad, J.; Watcharasit, P.; Becker, F. F. *Lab Chip* **2002**, *2*, 70-75.
(19) Gascoyne, P.; Satayavivad, J.; Ruchirawat, M. *Acta Trop.* **2004**, *89*, 357-369.
(20) Stephens, M.; Talary, M. S.; Pethig, R.; Burnett, A. K.; Mills, K. I. *Bone Marrow Transplantation* **1996**, *18*, 777-782.
(21) Talary, M. S.; Mills, K. I.; Hoy, T.; Burnett, A. K.; Pethig, R. *Med & Biol Eng & Comput* **1995**, *33*, 235-237.
(22) Green, N. G.; Morgan, H.; Milner, J. J. *Journal of Biochemical and Biophysical Methods* **1997**, *35*, 89-102.
(23) Morgan, H.; Green, N. G. *Journal of Electrostatics* **1997**, *42*, 279-293.
(24) Allsopp, D. W. E.; Milner, K. R.; Brown, A. P.; Betts, W. B. *Journal of Physics D: Applied Physics* **1999**, *32*, 1066-1074.
(25) Green, N. G.; Morgan, H. *Journal of Physics D: Applied Physics* **1997**, *30*, 2626-2633.
(26) Green, N. G.; Morgan, H. *Journal of Physics D: Applied Physics* **1997**, *30*, L41-L44.
(27) Pohl, H. A. *Dielectrophoresis*; Cambridge University Press: Cambridge, 1978.
(28) Benguigui, L.; Lin, I. J. *Journal of Physics D: Applied Physics* **1984**, *17*, L9-L12.
(29) Benguigui, L.; Lin, I. J. *Journal of Applied Physics* **1984**, *56*, 3294-3297.
(30) Lin, I. J.; Benguigui, L. *Journal of electrostatics* **1982**, *13*, 257-278.
(31) Lin, I. J.; Benguigui, L. *Separation Science and Technology* **1982**, *17(5)*, 645-654.
(32) Suehiro, J.; Zhou, G. B.; Imamura, M.; Hara, M. *IEEE Transactions On Industry Applications* **2003**, *39*, 1514-1521.
(33) Benguigui, L.; Lin, I. J. *Separation Science and Technology* **1982**, *17*, 1003-1017.
(34) Zhou, G.; Imamura, M.; Suehiro, J.; Hara, M., 37th Annual Meeting of the IEEE-Industry-Applications-Society, Pittsburgh, Pennsylvania 2002; Proc. IEEE; 1404-1411.
(35) Chou, C.-F.; Tegenfeldt, J. O.; Bakajin, O.; Chan, S. S.; Cox, E. C.; Darnton, N.; Duke, T.; Austin, R. H. *Biophys. J.* **2002**, *83*, 2170-2179.
(36) Lapizco-Encinas, B. H.; Simmons, B. A.; Cummings, E. B.; Fintschenko, Y. *Electrophoresis* **2004**, *25*, 1695-1704.
(37) Lapizco-Encinas, B. H.; Simmons, B. A.; Cummings, E. B.; Fintschenko, Y. *Analytical Chemistry* **2004**, *76*, 1571-1579.
(38) Xuan, X. C.; Xu, B.; Li, D. Q. *Analytical Chemistry* **2005**, *77*, 4323-4328.
(39) Shalom, A. L.; Lin, I. J. *Separation and Purification Methods* **1987**, *16*, 1-30.
(40) Shalom, A. L.; Lancelot, F.; Lin, I. J. *Separation Science and Technology* **1989**, *24*, 179-197.
(41) Chou, C.-F.; Zenhausern, F. *IEEE Engineering in Medicine and Biology Magazine* **2003**, *22*, 62-67.
(42) Cummings, E. B.; Singh, A. K. *Analytical Chemistry* **2003**, *75*, 4724-4731.
(43) Cummings, E. B. *IEEE Engineering in Medicine and Biology Magazine* **2003**, *22*, 75-84.
(44) Kirby, B. J.; Reichmuth, D. S.; Renzi, R. F.; Shepodd, T. J.; Wiedenman, B. J. *Lab Chip* **2005**, *5*, 184-190.
(45) Reichmuth, D. S.; Shepodd, T. J.; Kirby, B. J. *Analytical Chemistry* **2004**, *76*, 5063-5068.
(46) Fruetel, J. A.; Renzi, R. F.; VanderNoot, V. A.; Stamps, J.; West, J. A. A.; Ferko, S.; Crocker, R.; Bailey, C. G.; Arnold, D.; Wiedenman, B.; Choi, W.-Y.; Yee, D.; Shokair, I.; Hasselbrink, E.; Paul, P.; Rakestraw, D.; Padgen, D. *Electrophoresis* **2005**, *26*, 1144-1154.
(47) Fiechtner, G. J.; Cummings, E. B. *Anal. Chem.* **2003**, *75*, 4747-4755.
(48) Fiechtner, G. J.; Cummings, E. B. *Journal of Chromatography A* **2004**, *1027*, 245-257.
(49) Skulan, A. J.; Barrett, L. M.; Cummings, E. B.; Singh, A. K.; Fiechtner, G. J. *Submitted (Analytical Chemistry)* **2005**.

(50) Ausubel, F. M.; Brent, R.; Kingston, R. E.; Moore, D. D.; Seidman, J. G.; Smith, J. A.; Struhl, K. *Short Protocols in molecular Biology*, 5th ed.; Wiley: USA, 2002.
(51) Cummings, E. B. *Experiments in Fluids* **2000**, *29*, S42-S50.